PAPER

Check for updates

Unexpected bowing band evolution in an all-inorganic CsSn$_{1-x}$Pb$_x$Br$_3$ perovskite†

Yufan Xia,‡[a] Yuxuan Chen,‡[ab] Tian Luo,[a] Hongyao Liang,[a] Yujia Gao,[a] Xin Xu,[a] Weiguang Xie, [ID][a] Pengyi Liu,[a] Xin Wang, [ID][b] Yu-Jun Zhao [ID]*[c] and Tingting Shi [ID]*[a]

We theoretically investigated the structural and electronic properties of the all-inorganic perovskite CsSn$_{1-x}$Pb$_x$Br$_3$, compared with the mixed perovskite compound MA$_y$Cs$_{1-y}$Sn$_{1-x}$Pb$_x$Br$_3$, based on first-principle calculations. It has been demonstrated that Pb and Sn atoms are inclined to occupy the lattice sites uniformly in the all-inorganic perovskite, and this is distinguished from the most stable configurations observed in the mixed Cs-MA system. It is interesting that small Sn atoms prefer to stay close to the large MA$^+$ cations, leading to smaller local structural distortion. Through spin-orbital coupling calculations, we found non-linear bowing band evolution in the all-inorganic mixed Sn–Pb system with a small bowing parameter ($b = 0.35$), while the band gap of MA$_y$Cs$_{1-y}$Sn$_{1-x}$Pb$_x$Br$_3$ was clearly reduced as the ratio of MA was around 0.5 ($y \geq 0.25$). We determined the bowing band evolution in the mixed cation perovskites and the intrinsic electronic deficiency of the all-inorganic perovskite to obtain the optimal band gap.

Introduction

With the rapid development of photovoltaic materials, the power conversion efficiency (PCE) of perovskite solar cells has been swiftly improved to 25.2% within ten years,[1–5] resulting in photovoltaic power generation systems being in the spotlight in the research field. However, thermal and light stabilities still need to be stressed in the process of commercialization. Therefore, all-inorganic perovskite solar cells without hydrophilic organic cations have attracted increasing attention due to their outstanding thermal stability and phase stability.[6–11] Noticeably, the PCE of an all-inorganic perovskite obtained a rapid rise to 19.03%,[12] which has been predicted to approach the highest PCE record for a hybrid organic perovskite. Moreover, all-inorganic perovskites can be focused, due to their significant potentials in optical communication, safety monitoring, and biological sensing, by tuning the element compositions for wide applications.[13,14] All-inorganic perovskites consist of an ABX$_3$ structure, where cation A is selected to be the inorganic cation (Cs$^+$), atom B is a metal cation (Sn^{2+} or Pb^{2+}) and X is a halogen anion (Cl$^-$, Br$^-$ or I$^-$). Recent theoretical and experimental reports have shown that compositional engineering is an efficient strategy to suitably change the optoelectronic properties in order to aim for specific functionalities.[15,16] Considering the properties of photovoltaic materials, one important characteristic that a perovskite system should possess is the applicable band gap around the optimal value of 1.3–1.4 eV, according to the Shockley–Queisser (SQ) limitation.[17] Unfortunately, inorganic perovskites, such as CsPbI$_3$ and CsPbBr$_3$, both have wider band gaps ($E_g = 1.74$ eV and 2.34 eV, respectively),[9,18–20] implying that the maximum theoretical efficiency of these solar cells will be greatly restricted.

Previously, the mixture of cations and metal atoms were used to realize a higher stability and more suitable electronic properties in hybrid organic–inorganic perovskite solar cells. In 2014, Kanatzidis's group experimentally found the anomalous band gap behavior in a mixed Sn and Pb perovskite.[21] The energy band gaps of the mixed Pb–Sn perovskite following Vegard's law[22] were observed to be as low as around 1.1 eV, when the ratio of Pb : Sn was close to 1 : 1, thus broadening the light absorption into the near-infrared region. Furthermore, the antagonism phenomenon between the spin–orbit coupling (SOC) and the steric effect was investigated theoretically in MASn$_{1-x}$Pb$_x$I$_3$ materials.[23] The mixture of compositions can be applied to tune the electronic properties to enhance light absorption and PCE. In a recent experiment, Guo *et al.* reported a methodology for uniform Sn–Pb mixed perovskite films by a one-step blade coating method, yielding high efficiencies of over 15%.[24] The compositional engineering of mixing cations

[a]*Siyuan Laboratory, Guangzhou Key Laboratory of Vacuum Coating Technologies and New Energy Materials, Guangdong Provincial Engineering Technology Research Center of Vacuum Coating Technologies and New Energy Materials, Department of Physics, Jinan University, Guangzhou 510632, China. E-mail: ttshi@jnu.edu.cn*

[b]*National Center for International Research on Green Optoelectronics, South China Normal University, Guangzhou 510006, China*

[c]*Department of Physics, South China University of Technology, Guangzhou, Guangdong 510640, China. E-mail: zhaoyj@scut.edu.cn*

† Electronic supplementary information (ESI) available. See DOI: 10.1039/d0ra03709e

‡ These authors contribute equally to this work.

can be used to flexibly tune the optoelectronic properties, and thus increase the PCE.

In this paper, we aim to theoretically reveal insight into the band gap bowing effect that is introduced by the mixing of Sn and Pb metal atoms in an all-inorganic perovskite. The structural and optoelectronic configurations of the all-inorganic $CsSn_{1-x}Pb_xBr_3$ and $MA_yCs_{1-y}Sn_{1-x}Pb_xBr_3$ perovskites are systematically calculated based on density functional theory. We found that Pb and Sn atoms prefer to occupy dispersedly in the all-inorganic $CsSn_{1-x}Pb_xBr_3$ system, and this is different to in the mixed cation $MA_yCs_{1-y}Sn_{1-x}Pb_xBr_3$ system. The obvious bowing band evolutions were found in the mixed perovskite system when SOC calculations were employed. Based on all the calculated band gap values, the fit curves showed a non-linear changing trend of the band gaps for each perovskite system, following Vegard's law. Intriguingly, the band gap cannot be significantly reduced in the all-inorganic Sn–Pb perovskite compounds, due to it having the smallest bowing parameter value, compared with the larger bowing parameter values in the MA–Cs mixed systems. Therefore, the deficiency of electronic properties in the all-inorganic perovskite is difficult to overcome through compositional engineering, unlike in the case of bowing band evolution in the hybrid organic perovskite materials.

Methods

In this study, all calculations were performed using the Vienna *ab initio* simulation package (VASP),[25] based on density functional theory (DFT). The projector augmented wave (PAW)[26] pseudopotentials were used within the Perdew–Burke–Ernzerhof (PBE) functional[27,28] for the exchange–correlation functional. The plane-wave cutoff energy for the basis was set to 400 eV. A $2 \times 2 \times 2$ supercell and a Monkhorst–Pack $3 \times 3 \times 3$ k-point mesh in first Brillouin zone[29] integrations were carried out within supercell calculations. Heyd–Scuseria–Ernzerhof (HSE03)[30] and PBE0[31] hybrid functionals were also employed for further calculations. Additionally, all structures were constructed in the cubic phase to save computational time. Four high-symmetric k-points were included for the band structures calculation: G (0, 0, 0), X (0, 1/2, 0), M (1/2, 1/2, 0), and R (1/2, 1/2, 1/2). The atomic positions were relaxed until the energy converged within 10^{-4} eV and the absolute values of the force on the atoms were less than 0.02 eV Å^{-1}. Due to the involvement of the heavy metal Pb, the spin–orbit coupling (SOC)[32,33] effect was considered in our calculations. It is of great importance to calculate the perovskite systems using GGA + SOC and PBE0 + SOC. Although the method of GGA + SOC underestimates the value of the bandgap,[34] it presents the changing trend of the band evolution accurately. All crystal structures were constructed by VESTA.[35]

Results and discussion

Fig. 1(a) and (b) show the most stable and metastable crystal structures of $MA_{0.5}Cs_{0.5}Sn_{0.5}Pb_{0.5}Br_3$. After relaxation, the perovskite structure is distorted slightly when mixing MA and Cs, leading to a pseudo-cubic phase. The crystal structures of the most stable and the metastable $CsSn_{0.5}Pb_{0.5}Br_3$ states are shown in Fig. 1(c) and (d) with the space group $Pm\bar{3}m$. It is clear that the occupation sites of the Pb and Sn metal atoms in the most stable configurations are opposite for $CsSn_{0.5}Pb_{0.5}Br_3$ and $MA_{0.5}Cs_{0.5}Sn_{0.5}Pb_{0.5}Br_3$. In other words, the Pb and Sn metal atoms are occupied dispersedly in the most stable configuration of $CsSn_{0.5}Pb_{0.5}Br_3$, while they are clustered together in the most
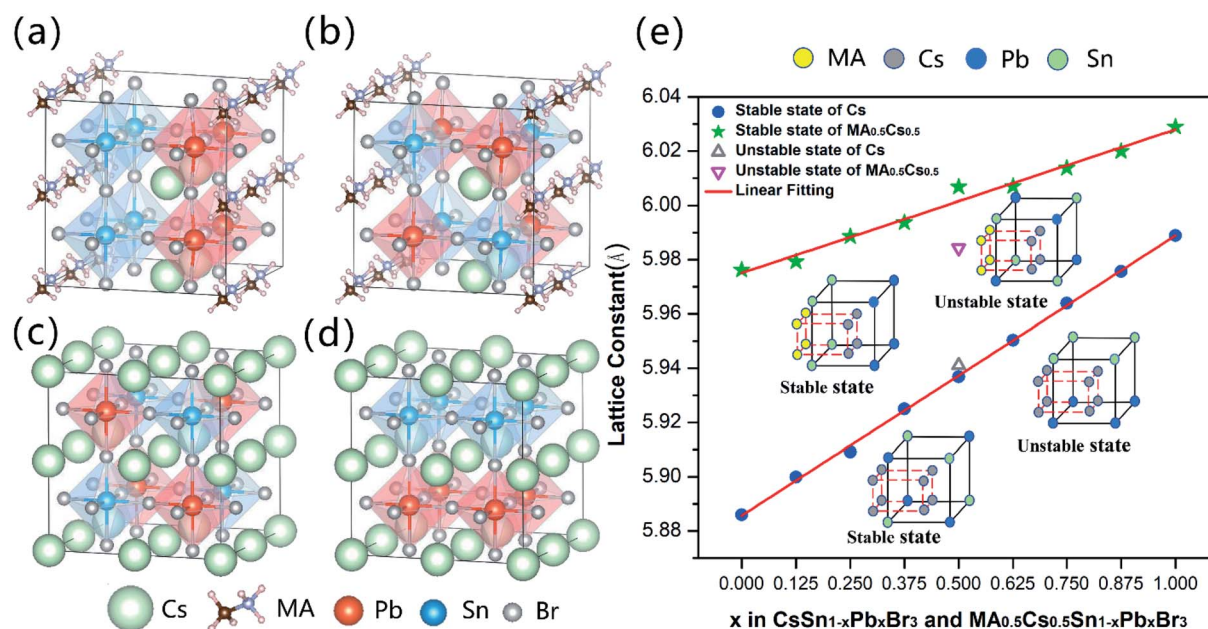

Fig. 1 Schematic diagrams of the crystal structures of (a) the most stable configuration of $MA_{0.5}Cs_{0.5}Sn_{0.5}Pb_{0.5}Br_3$, (b) the metastable configuration of $MA_{0.5}Cs_{0.5}Sn_{0.5}Pb_{0.5}Br_3$, (c) the most stable configuration of $CsSn_{0.5}Pb_{0.5}Br_3$, and (d) the metastable configuration of $CsSn_{0.5}Pb_{0.5}Br_3$. (e) Trends of the calculated lattice constants of $MA_{0.5}Cs_{0.5}Sn_{1-x}Pb_xBr_3$ and $CsSn_{1-x}Pb_xBr_3$ as functions of composition x.
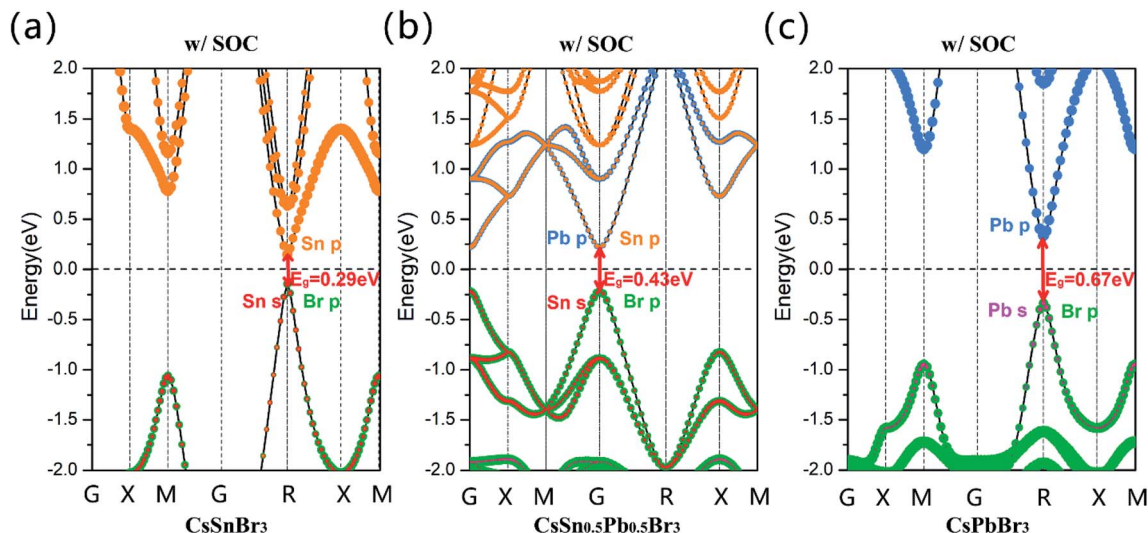
Fig. 2 Calculated projected band structures of (a) $CsSnBr_3$, (b) $CsSn_{0.5}Pb_{0.5}Br_3$, and (c) $CsPbBr_3$ obtained by the GGA + SOC method. The Fermi level was set at 0 eV and is denoted as a black dashed line.

stable configuration of the $MA_{0.5}Cs_{0.5}Sn_{0.5}Pb_{0.5}Br_3$ system. Other stable mixed configurations are illustrated in Fig. S1 (ESI).† This interesting phenomenon is related to the larger size of the MA^+ cations. Clearly, the small Sn atoms of the stable configurations of the $MA_yCs_{1-y}Sn_{1-x}Pb_xBr_3$ $(0 < y \leq 0.5)$ compound tend to stay close to the MA^+ cations to reduce the local structural distortion (as seen in Fig. S1 (ESI)†). As shown in Fig. 1(e), we further found that the lattice constants of the stable systems vary linearly with the increase of Pb^{2+} ion content, satisfying Vegard's law. Nevertheless, the lattice constants of the metastable systems deviate from the linear fitting line. In order to clarify the relative occupied sites of the metal atoms, we used a schematic diagram to elucidate the different atomic positions between the stable configurations and the metastable configurations (inset of Fig. 1(e)). Details of the lattice constants can be seen in Table S2 (ESI).†

In addition, the Goldschmidt tolerance factor is a crucial index in predicting the stability of halide perovskites: $t_{eff} = (r_A) + (r_B)/[\sqrt{2}(r_B + r_X)]$, where r is the ionic radius.[36,37] A tolerance factor of within 0.9–1.0 is an ideal stable cubic structure in perovskite materials. It is known that increasing the radius of A (r_A) and decreasing the radius of B (r_B) are important and effective strategies to improve the stability of perovskites. Hence, a larger cation (MA^+) mixed with Cs^+ and a smaller metal cation (Sn^{2+}) alloyed with Pb^{2+} are necessary to investigate. The t_{eff} ($Cs^+ = 1.88$ Å, $Sn^{2+} = 1.12$ Å, $Pb^{2+} = 1.19$ Å, and $Br^- = 1.96$ Å)[38] value of $CsSnBr_3$ (0.882) is larger than that of $CsPbBr_3$ (0.862), indicating that $CsSnBr_3$ as the possible candidate is more stable for the photovoltaic application of inorganic perovskites.

Subsequently, we calculated projected band structures of $CsSnBr_3$, $CsSn_{0.5}Pb_{0.5}Br_3$ and $CsPbBr_3$, and these are displayed in Fig. 2(a)–(c), through GGA + SOC methods (w/SOC). The
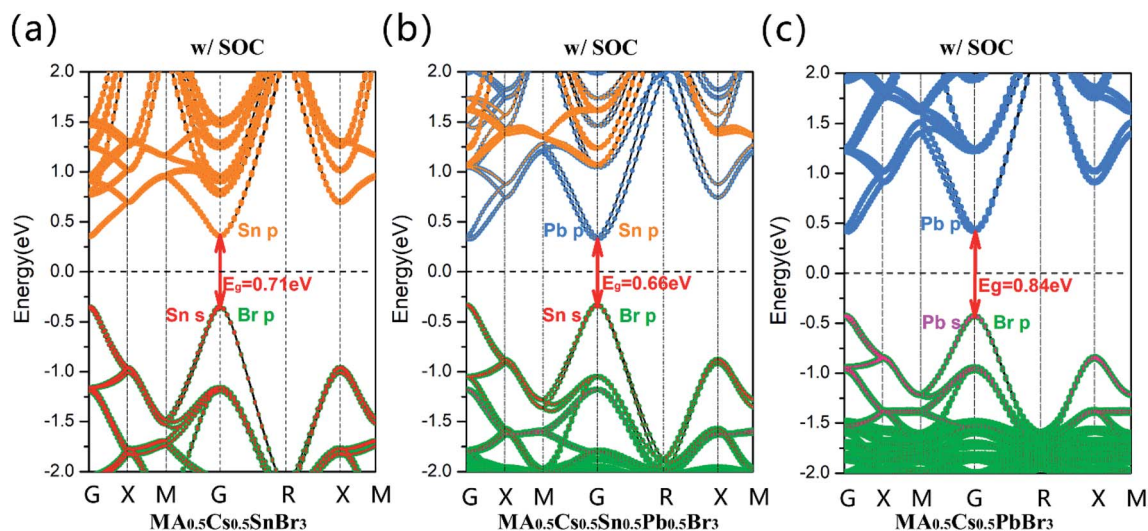

Fig. 3 Calculated projected band structures of (a) $MA_{0.5}Cs_{0.5}SnBr_3$, (b) $MA_{0.5}Cs_{0.5}Sn_{0.5}Pb_{0.5}Br_3$, and (c) $MA_{0.5}Cs_{0.5}PbBr_3$ obtained by the GGA + SOC method. The Fermi level was set at 0 eV and is denoted as a black dashed line.
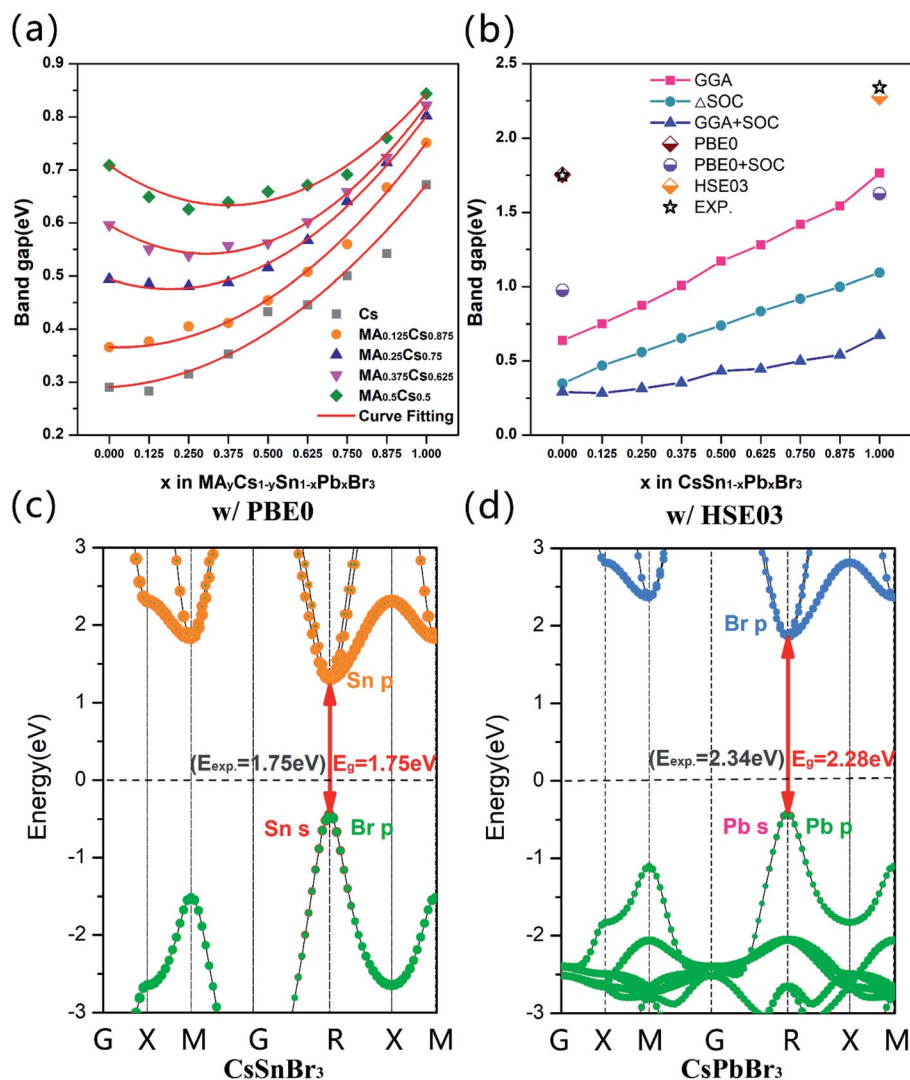
Fig. 4 (a) Calculated band gap evolutions of $MA_yCs_{1-y}Sn_{1-x}Pb_xBr_3$ as functions of the compositions of x and y. (b) Calculated band gap evolutions of $CsSn_{1-x}Pb_xBr_3$ as functions of the compositions of x. Calculated projected band structures of (c) $CsSnBr_3$ obtained by the PBE0 method (w/PBE0), and (d) $CsPbBr_3$ obtained by the HSE03 method (w/HSE03). The Fermi level was set at 0 eV and is denoted as a black dashed line.

Sn-5s, Sn-5p, Pb-6s, Pb-6p and Br-4p orbitals are highlighted in red, orange, pink, blue and green, respectively. It can be clearly seen that the band gap calculated by GGA + SOC gradually increases with the addition of the Pb^{2+} cation and the projected band structure indicates that the Sn-5s, Pb-6s and Br-4p orbitals contribute most to the valence band maximum (VBM) state, and the conduction band minimum (CBM) state is dominated by the Sn-5p and Pb-6p orbitals. It is clear that the bandgap of $CsSn_{0.5}Pb_{0.5}Br_3$ is not smaller than that of $CsSnBr_3$.

However, for the $MA_{0.5}Cs_{0.5}Sn_{0.5}Pb_{0.5}Br_3$ system, its band gap (GGA + SOC: 0.66 eV) is clearly lower than that of the pure Sn and pure Pb configurations, as shown in Fig. 3(b). There is an anomalous band gap evolution after the addition of the MA^+ ion. From the projected band structures, we found that both Sn-5p and Pb-6p orbitals contribute to the CBM in $MA_{0.5}Cs_{0.5}$-$Sn_{0.5}Pb_{0.5}Br_3$. Herein, the band gap in the $MA_{0.5}Cs_{0.5}SnBr_3$

compound is 0.71 eV, as shown in Fig. 3(a), and the band gap in the $MA_{0.5}Cs_{0.5}PbBr_3$ compound is 0.84 eV, as shown in Fig. 3(c).

Considering the alloy of the Sn–Pb systems studied in our calculations, according to Vegard's law, we quantificationally fit the band bowing curves and obtained the corresponding bowing parameter b values. The band gap of mixing A and B atoms can be estimated using the relationship below:[39–41]

$$E_g(A_{1-x}B_x) = (1-x)E_g(A) + xE_g(B) - bx(1-x) \quad (1)$$

where x and $1-x$ represent the composition ratio of Pb and Sn, respectively, and b represents the bowing parameter that causes a deviation from the simple linear trend. Fig. 4(a) displays the band gap of different MA^+ ratios of the bowing band evolutions. With an increase of the MA^+ ratio, the bowing trend changes differently and the bowing parameters keep increasing from 0.35 to 0.54 [Table 1]. The varying values of the bowing

Table 1 Fitting quadratic equations and bowing parameters of the $MA_yCs_{1-y}Sn_{1-x}Pb_xBr_3$ systems

System	Fitting quadratic equation	Bowing parameter
$CsSn_{1-x}Pb_xBr_3$	$E_g = 0.35x^2 + 0.032x + 0.29$	0.35
$MA_{0.125}Cs_{0.875}Sn_{1-x}Pb_xBr_3$	$E_g = 0.41x^2 - 0.025x + 0.37$	0.41
$MA_{0.25}Cs_{0.75}Sn_{1-x}Pb_xBr_3$	$E_g = 0.50x^2 - 0.19x + 0.49$	0.50
$MA_{0.375}Cs_{0.625}Sn_{1-x}Pb_xBr_3$	$E_g = 0.58x^2 - 0.35x + 0.60$	0.58
$MA_{0.5}Cs_{0.5}Sn_{1-x}Pb_xBr_3$	$E_g = 0.54x^2 - 0.40x + 0.71$	0.54

parameter b depend on the different compounds. The specific mixed atoms in the compound often have an effect on the band evolution. For instance, the band gap evolution of $ZnS_{1-x}Se_x$ is close to the linear trend, differentiating from the distinct bowing band of $ZnSe_{1-x}Te_x$.[42] In our calculations, when the ratio of MA^+ was more than 0.125 ($y > 0.125$), the band gaps of the Sn–Pb compounds could be reduced to smaller than those of the two extremes in the pure Sn and Pb states, and the decreasing trend of the band gap occurred when the ratio of Pb was tuned to within the range of $0 \leq x \leq 0.25$. The band gap
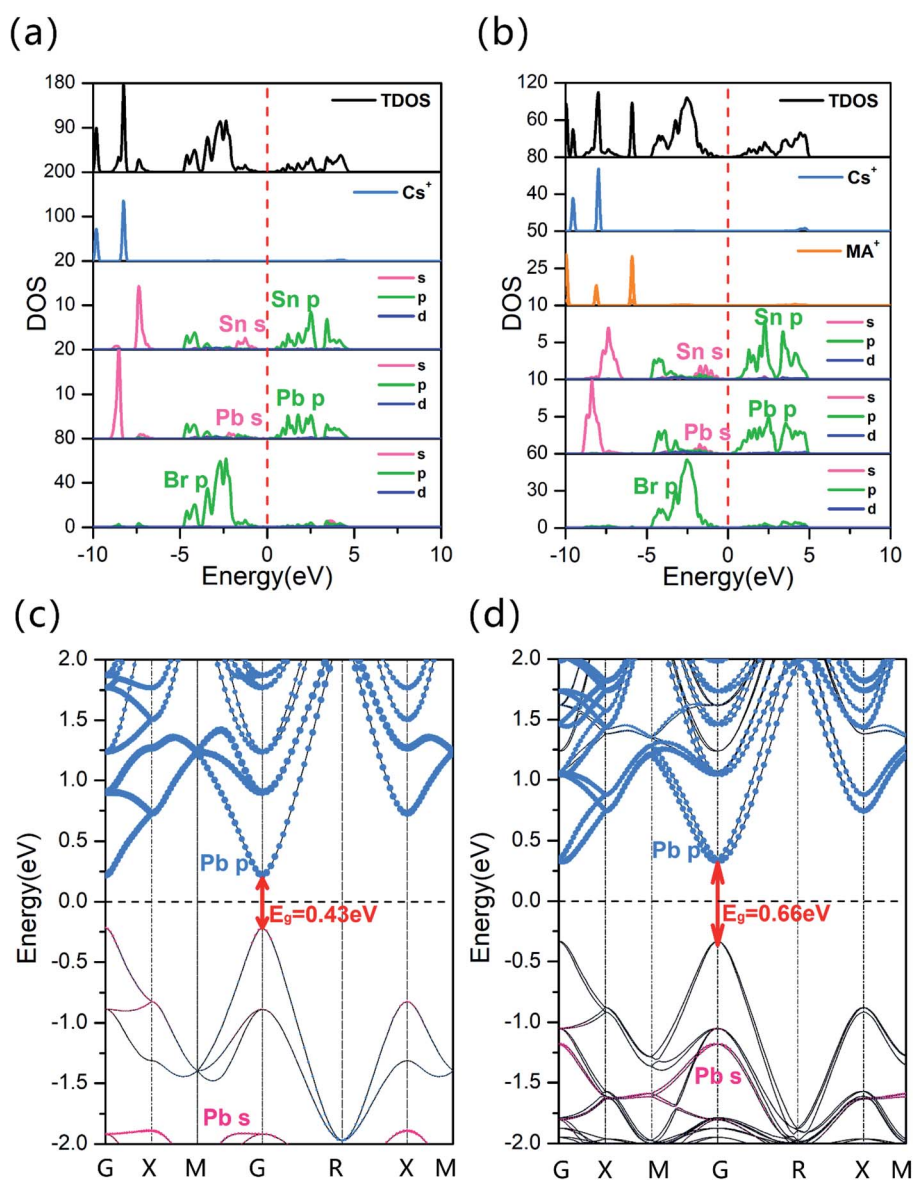

Fig. 5 TDOS and PDOS of (a) $CsSn_{0.5}Pb_{0.5}Br_3$ and (b) $MA_{0.5}Cs_{0.5}Sn_{0.5}Pb_{0.5}Br_3$. Calculated projected band structures of (c) $CsSn_{0.5}Pb_{0.5}Br_3$ and (d) $MA_{0.5}Cs_{0.5}Sn_{0.5}Pb_{0.5}Br_3$ obtained by the GGA + SOC method.

reached a minimum value at $x = 0.25$ for the $MA_{0.25}Cs_{0.75}Sn_{0.75}Pb_{0.25}Br_3$ and $MA_{0.375}Cs_{0.625}Sn_{0.75}Pb_{0.25}Br_3$ compounds. Similarly, the electronic properties of $MA_{0.5}Cs_{0.5}Sn_{1-x}Pb_xBr_3$ also indicated a clear bowing band tendency and a large decrease in the band gaps by tuning the ratio of Sn atoms. Therefore, it was interesting to find that the bowing effect of the band gap was more evident with an increase of MA^+ cations in the mixed Sn–Pb perovskites. We have described the relationship among the band gaps using the GGA method with SOC, without SOC and the reduction values of SOC of $CsSn_{1-x}Pb_xBr_3$ as a function of x in Fig. 4(b). It can clearly be seen that the band gap evolutions of GGA and ΔSOC are linear. ΔSOC displays the effect of SOC that causes non-linear band evolution under GGA + SOC calculations. Additionally, we further considered the influence of vdW interactions in the $MA_{0.5}Cs_{0.5}Sn_{1-x}Pb_xBr_3$ system and determined similar band evolution. The band gaps considering the vdW interactions are slightly larger than those without taking vdW interactions into account (as seen in Fig. S7 (ESI)†). Systems of band trends containing MA^+ cations are displayed in Fig. S5 and S6 (ESI).† Furthermore, hybrid functionals (PBE0 and HSE03) were used to calculate the band structures of the pure Sn and Pb systems and these are shown in Fig. 4(c) and (d). The band gaps of $CsSnBr_3$ and $CsPbBr_3$ using the PBE0 and HSE03 methods, respectively, are 1.75 eV and 2.28 eV, and these results are in line with the experimental values.[43,44] In addition, the orbital compositions of the VBM and CBM states are consistent with the previous results of the GGA + SOC calculations. This further proves that the changing trends of the band evolution of the $CsSn_{1-x}Pb_xBr_3$ perovskite were correctly summarized here. A similar methodology has already been employed to predict the band bowing trend of the mixed Sn–Pb perovskite system.[23]

Fig. 5 presents the total density of states (TDOS) and projected density of states (PDOS) using the GGA + SOC method. In all cases, the dominant components of the band edges are similar. The CBM mainly consists of the Sn-5p and Pb-6p electronic states and the VBM is derived from the Sn-5s and Br-4p orbitals, because the original orbital of Sn-5s is higher than the Pb-6s orbital. It is worth noting that the Pb-6s orbitals contribute to the different components of the valance band (VB), as shown in Fig. 5(c) and (d). By comparing the same mixture ratio of the Sn–Pb compounds, we found that the Pb-6s orbital contributes to the lower energy states of the VB in $CsSn_{0.5}Pb_{0.5}Br_3$, whilst for $MA_{0.5}Cs_{0.5}Sn_{0.5}Pb_{0.5}Br_3$ it contributes to the higher energy levels. This also means that the main component of the VBM, the Sn-5s orbitals, are pushed higher in the $MA_{0.5}Cs_{0.5}Sn_{0.5}Pb_{0.5}Br_3$ perovskite, reducing its band gap to $x = 0.5$. Through studying these all-inorganic systems, it can be seen that a change in the mixture ratio does not affect the bowing parameter due to its distinguished structural configuration. As a result, a reduction in the band gap, in order to obtain a smaller optimal E_g value, is restricted in an all-inorganic perovskite. Furthermore, the PDOS of $CsSn_{0.5}Pb_{0.5}Br_3$ and $MA_{0.5}Cs_{0.5}Sn_{0.5}Pb_{0.5}Br_3$, as seen in Fig. 5(a) and (b), were calculated and the results stated that the Pb-6s states deviated from the VBM, which is lower in the $CsSn_{0.5}Pb_{0.5}Br_3$ system, as indicated by the pink lines.

Conclusions

In summary, we have investigated the structural and electronic properties of the all-inorganic perovskite $CsSn_{1-x}Pb_xBr_3$ and $MA_yCs_{1-y}Sn_{1-x}Pb_xBr_3$ materials. Noticeably, our calculations demonstrated that the occupation sites of the Sn and Pb atoms show distinguishable features in these two mixed compounds. For the all-inorganic $CsSn_{1-x}Pb_xBr_3$ perovskite, the Sn and Pb atoms preferred to remain scattered in the most stable configuration. The structural characteristics of the inorganic perovskite influenced its electronic properties, and this was eminent in the $MA_yCs_{1-y}Sn_{1-x}Pb_xBr_3$ perovskite. It was interesting to discover that the bowing band parameter of $CsSn_{1-x}Pb_xBr_3$ was the smallest amongst all the perovskite materials studied. As a result, an unexpected electronic deficiency was observed in $CsSn_{1-x}Pb_xBr_3$, as the band gap of the Sn–Pb mixed structures cannot be reduced significantly for the ideal theoretical PCE. Herein, we provide fundamental understanding of the influence of cations on bowing band evolution and a useful strategy for tuning the electronic properties of mixed perovskite systems.

Conflicts of interest

The authors declare no competing financial interests.

Acknowledgements

References

1 A. Kojima, K. Teshima, Y. Shirai and T. Miyasaka, *J. Am. Chem. Soc.*, 2009, **131**, 6050–6051.

2 H. S. Kim, C. R. Lee, J. H. Im, K. B. Lee, T. Moehl, A. Marchioro, S. J. Moon, R. Humphry-Baker, J. H. Yum, J. E. Moser, M. Grätzel and N. G. Park, *Sci. Rep.*, 2012, **2**, 1–7.

3 W. S. Yang, J. H. Noh, N. J. Jeon, Y. C. Kim, S. Ryu, J. Seo and S. Il Seok, *Science*, 2015, **348**, 1234–1237.

4 D. Bi, C. Yi, J. Luo, J.-D. Décoppet, F. Zhang, S. M. Zakeeruddin, X. Li, A. Hagfeldt and M. Grätzel, *Nat. Energy*, 2016, **1**, 16142.

5 *Best Research-Cell Efficiency Chart*, http://www.nrel.gov/pv/cell-efficiency.html, accessed, June 16, 2020.

6 T. Zhang, M. I. Dar, G. Li, F. Xu, N. Guo, M. Grätzel and Y. Zhao, *Sci. Adv.*, 2017, **3**, 1–7.

7 Y. Chen, T. Shi, P. Liu, W. Xie, K. Chen, X. Xu, L. Shui, C. Shang, Z. Chen, H. L. Yip, G. Zhou and X. Wang, *J. Mater. Chem. A*, 2019, **7**, 20201–20207.

8 J. Wang, J. Zhang, Y. Zhou, H. Liu, Q. Xue, X. Li, C. C. Chueh, H. L. Yip, Z. Zhu and A. K. Y. Jen, *Nat. Commun.*, 2020, **11**, 1–9.

9 M. Kulbak, S. Gupta, N. Kedem, I. Levine, T. Bendikov, G. Hodes and D. Cahen, *J. Phys. Chem. Lett.*, 2016, **7**, 167–172.

10 C. Liu, W. Li, C. Zhang, Y. Ma, J. Fan and Y. Mai, *J. Am. Chem. Soc.*, 2018, **140**, 3825–3828.

11 C. Y. Chen, H. Y. Lin, K. M. Chiang, W. L. Tsai, Y. C. Huang, C. S. Tsao and H. W. Lin, *Adv. Mater.*, 2017, **29**, 1–7.

12 Y. Wang, X. Liu, T. Zhang, X. Wang, M. Kan, J. Shi and Y. Zhao, *Angew. Chem., Int. Ed.*, 2019, **58**, 16691–16696.

13 Y. Dong, Y. Gu, Y. Zou, J. Song, L. Xu, J. Li, J. Xue, X. Li and H. Zeng, *Small*, 2016, **12**, 5622–5632.

14 Y. Ling, Y. Tian, X. Wang, J. C. Wang, J. M. Knox, F. Perez-Orive, Y. Du, L. Tan, K. Hanson, B. Ma and H. Gao, *Adv. Mater.*, 2016, **28**, 8983–8989.

15 N. K. Kumawat, A. Dey, A. Kumar, S. P. Gopinathan, K. L. Narasimhan and D. Kabra, *ACS Appl. Mater. Interfaces*, 2015, **7**, 13119–13124.

16 Z. Yang, X. Zhang, W. Yang, G. E. Eperon and D. S. Ginger, *Chem. Mater.*, 2020, **32**, 2782–2794.

17 W. Shockley and H. J. Queisser, *J. Appl. Phys.*, 1961, **32**, 510–519.

18 A. Swarnkar, A. R. Marshall, E. M. Sanehira, B. D. Chernomordik, D. T. Moore, J. A. Christians, T. Chakrabarti and J. M. Luther, *Science*, 2016, **354**, 92–95.

19 Z. Guan, Y. Wu, P. Wang, Q. Zhang, Z. Wang, Z. Zheng, Y. Liu, Y. Dai, M. H. Whangbo and B. Huang, *Appl. Catal., B*, 2019, **245**, 522–527.

20 E. M. Sanehira, A. R. Marshall, J. A. Christians, S. P. Harvey, P. N. Ciesielski, L. M. Wheeler, P. Schulz, L. Y. Lin, M. C. Beard and J. M. Luther, *Sci. Adv.*, 2017, **3**, eaao4204.

21 F. Hao, C. C. Stoumpos, R. P. H. Chang and M. G. Kanatzidis, *J. Am. Chem. Soc.*, 2014, **136**, 8094–8099.

22 A. R. Denton and N. W. Ashcroft, *Phys. Rev. A*, 1991, **43**, 3161–3164.

23 J. Im, C. C. Stoumpos, H. Jin, A. J. Freeman and M. G. Kanatzidis, *J. Phys. Chem. Lett.*, 2015, **6**, 3503–3509.

24 L. Zeng, Z. Chen, S. Qiu, J. Hu, C. Li, X. Liu, G. Liang, C. J. Brabec, Y. Mai and F. Guo, *Nano Energy*, 2019, **66**, 104099.

25 G. Kresse and J. Furthmüller, *Phys. Rev. B*, 1996, **54**, 11169–11186.

26 G. Kresse and D. Joubert, *Phys. Rev. B*, 1999, **59**, 1758–1775.

27 J. P. Perdew, K. Burke and M. Ernzerhof, *Phys. Rev. Lett.*, 1996, **77**, 3865–3868.

28 J. P. Perdew and W. Yue, *Phys. Rev. B*, 1986, **33**, 8800–8802.

29 J. D. Pack and H. J. Monkhorst, *Phys. Rev. B*, 1976, **13**, 5188–5192.

30 J. Heyd, G. E. Scuseria and M. Ernzerhof, *J. Chem. Phys.*, 2003, **118**, 8207–8215.

31 C. Adamo and V. Barone, *J. Chem. Phys.*, 1999, **110**, 6158–6170.

32 E. Narsimha Rao, G. Vaitheeswaran, A. H. Reshak and S. Auluck, *Phys. Chem. Chem. Phys.*, 2017, **19**, 31255–31266.

33 J. Even, L. Pedesseau, J. M. Jancu and C. Katan, *J. Phys. Chem. Lett.*, 2013, **4**, 2999–3005.

34 C. Filippi, D. J. Singh and C. J. Umrigar, *Phys. Rev. B*, 1994, **50**, 14947–14951.

35 K. Momma and F. Izumi, *J. Appl. Crystallogr.*, 2008, **41**, 653–658.

36 V. M. Goldschmidt, *Naturwissenschaften*, 1926, **14**, 477–485.

37 A. Swarnkar, W. J. Mir and A. Nag, *ACS Energy Lett.*, 2018, **3**, 286–289.

38 R. D. Shannon, *Acta Crystallogr., Sect. A*, 1976, **32**, 751–767.

39 M. Wang, G. T. Fei, Y. G. Zhang, M. G. Kong and L. De Zhang, *Adv. Mater.*, 2007, **19**, 4491–4494.

40 J. A. Van Vechten and T. K. Bergstresser, *Phys. Rev. B*, 1970, **1**, 3351–3358.

41 A. A. El-Shazly, M. M. H. El-Naby, M. A. Kenawy, M. M. El-Nahass, H. T. El-Shair and A. M. Ebrahim, *Appl. Phys. A*, 1985, **36**, 51–53.

42 S. Larach, R. E. Shrader and C. F. Stocker, *Phys. Rev.*, 1957, **108**, 587–589.

43 D. Sabba, H. K. Mulmudi, R. R. Prabhakar, T. Krishnamoorthy, T. Baikie, P. P. Boix, S. Mhaisalkar and N. Mathews, *J. Phys. Chem. C*, 2015, **119**, 1763–1767.

44 J. Liang, P. Zhao, C. Wang, Y. Wang, Y. Hu, G. Zhu, L. Ma, J. Liu and Z. Jin, *J. Am. Chem. Soc.*, 2017, **139**, 14009–14012.